



ELSEVIER

Contents lists available at ScienceDirect

Journal of the Mechanics and Physics of Solids

journal homepage: www.elsevier.com/locate/jmps

Bending of single crystal microcantilever beams of cube orientation: Finite element model and experiments

Eralp Demir*, Franz Roters, Dierk Raabe

Max-Planck-Institut für Eisenforschung, Max-Planck Str. 1, 40237 Düsseldorf, Germany

ARTICLE INFO

Article history:

Received 15 December 2009

Received in revised form

24 June 2010

Accepted 5 July 2010

Keywords:

Cube orientation

Single crystal

Bending size effect

Strain gradient hardening

Crystal plasticity

ABSTRACT

The aim of this work is to investigate the microstructure evolution, stress–strain response and strain hardening behavior of microscale beams. For that purpose, two single crystal cantilever beams in the size dependent regime were manufactured by ion beam milling and beams were bent with an indenter device. A crystal plasticity material model for large deformations was implemented in a finite element framework to further investigate the effect of boundary constraints. Simulations were performed using bulk material properties of single crystal copper without any special treatment for the strain gradients. The difference between the slopes of the experimental and the simulated force displacement curves suggested negligible amount of strain gradient hardening compared to the statistical hardening mechanisms.

© 2010 Elsevier Ltd. All rights reserved.

1. Introduction

Bending is an alternative small scale testing method to pillar compression and indentation. It is advantageous compared to pillar compression in which both the surface of the tool and the top surface of the sample must be strictly parallel to each other (Volkert and Lilleodden, 2006; Greer et al., 2005; Shade et al., 2009; Uchic et al., 2006; Nix et al., 2007) and to indentation which has a complicated deformation geometry. In addition, bending allows the deformed region to be studied far away from the tool contact zone, hence free of contact and friction effects.

In recent cantilever beam bending experiments, size dependent flow stresses were measured (Demir et al., 2010; Gong and Wilkinson, 2009; Motz et al., 2005). Stolken and Evans performed uniform bending experiments on Ni polycrystal thin films having a thickness range of 12.5–50 μm (Stolken and Evans, 1998) and they related the size dependence of normalized bending moment to the strain gradients. In the Demir et al. (2010), size dependent flow stresses were measured during bending of cantilevers of single crystals and shear localizations were found from the electron backscatter diffraction (EBSD) measurements. The size dependence of the yield strengths in the Demir et al. (2010) was explained with a mean field breakdown theory for beams that were thinner than 1 μm . They concluded that cantilever beam bending can be used as a reliable means to characterize strength of materials at micro scale.

Size dependence of strain hardening was related to the strain gradients in deformations that involve plastic curvature of crystal lattice (Stolken and Evans, 1998; Fleck et al., 1994; Shi et al., 2008). In those works, strain gradients were expressed in terms of the dislocation densities using the gradients of either the lattice shear (Ashby, 1970) or the lattice rotations (Nye, 1953). The strain gradient hardening is included to the models using Taylor relation as in the Wang et al. (2007) and

* Corresponding author. Current address: 191 Rhodes Hall, Cornell University, Ithaca, NY 14853, USA.

E-mail addresses: ed297@cornell.edu, eralpdemir1@yahoo.com (E. Demir).

Nix and Gao (1998). Therefore, strain gradients were believed to be the source of size dependence of mechanical strength for bending at microscale (Stolken and Evans, 1998).

To gain a better understanding of bending at microscale and to search for the effect of strain gradients, a critical bending experiment was designed and finite element simulations were performed. Two single crystal cantilever beams of cube orientation having approximate thicknesses of 5 μm were manufactured by ion beam milling. Each beam was loaded in an indenter setup with a different moment arm. Ex situ EBSD measurements were performed to investigate the microstructural evolution after each displacement increment. The anisotropic elastic and elastic–plastic behavior of the crystal was implemented in a commercial finite element software to simulate the force displacement behavior and to model the strain distributions inside the beams for the same real test sample geometry with the actual boundary constraints. A conventional crystal plasticity model was implemented to incorporate the strain localization effects (Asaro and Rice, 1977) as observed in the experiments (Demir et al., 2010). The hardening contribution from the strain gradients was neglected in the model and a constitutive law using bulk single crystal material properties was utilized. The beam thickness was selected in the size effected regime (Demir et al., 2010; Motz et al., 2005; Stolken and Evans, 1998) to investigate the effect of strain gradients. For that purpose, the simulated and experimentally measured strain hardening responses were compared as obtained from the force displacement curves.

2. Experiments

2.1. Details of experimental procedure

Copper single crystals were produced by directional solidification in a Bridgeman furnace by the use of a cube oriented seed crystal. Rectangular samples were cut by wire electro discharge machining. The two surfaces of the sample were first wet ground and then polished with diamond pastes of 3 and 1 μm , respectively. The top surface of the sample was electro polished with D2 solution of Struers using default device settings for copper.

Fig. 1 shows the final dimensions of the beam after focused ion beam (FIB) milling. All dimensions were machined using grazing incident milling in order to minimize the ion beam damage (Kiener et al., 2007). Final milling current was 100 pA at 30 keV emission voltage.

Table 4 shows the important final dimensions of the beams after milling. t_{ext} , t_{int} , w , l and y refer to exterior thickness, interior thickness, width, length and moment arm, respectively. The beam width was greater than three times the thickness in order to ensure plain strain deformation. Moreover the taper along the width of the beams was minimized by additionally tilting the beams $\pm 1.5^\circ$ with respect to the FIB milling axis. However, there was 0.6–0.7 μm thickness variation as a manufacturing error due to the curved geometry of the ion beam over long milling distances of 15–17 μm . The average thickness of the beams was nearly 5 μm in order to minimize the effect of damaged layer by ion milling (50 nm thick layer for a milling current of 1 nA at 30 keV from Kiener et al., 2007) and to remain away from the dislocation source limitation regime (Demir et al., 2010).

Average Euler angles of $\varphi_1 = 1.4^\circ$, $\Phi = 3.1^\circ$ and $\varphi_2 = 8.0^\circ$ (Bunge notation) were measured before loading the beams, Fig. 2, with an average noise of approximately 0.2° .

Beams were bent with two different moment arms in an indenter as in Table 1. Beams a and b refer to the beams with moment arms of 12.1 ± 0.1 and 5.2 ± 0.1 μm , respectively. A cono-spherical indenter tip of diamond with 5 μm radius (Hys Ti-45) was used in the experiments. The indenter was located using the piezo-scanning tool with the indenter tip. An approximate offset, z , from the center of the beams of 1.5 μm was measured as a positioning inaccuracy. The indenter tip radius was selected as large as possible to minimize the indentation of the surface of the beams while it allowed the use of piezo-scanning for accurate positioning. The beams were loaded interruptly with a displacement increment of 1 μm while a constant displacement rate of 0.1 $\mu\text{m/s}$ was maintained (displacement controlled). Ex situ SEM and EBSD measurements were performed after each displacement increment.

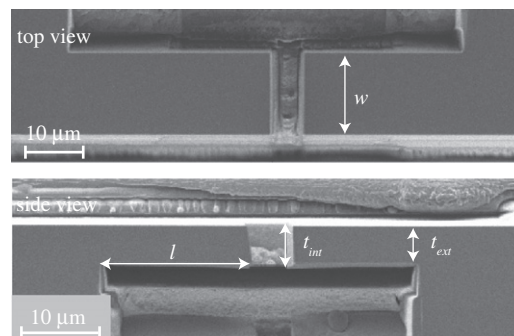


Fig. 1. Dimensions measured from the top and the side views of the beams before loading. w , l , t_{int} , t_{ext} refer to the width, length, thickness at the exterior and the interior surfaces, respectively.

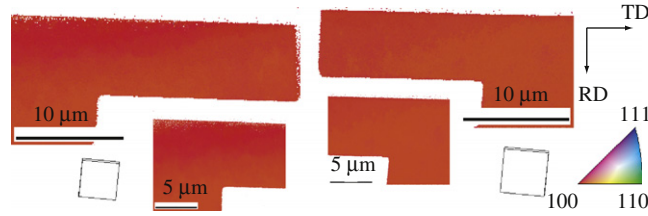


Fig. 2. Inverse pole figure maps of the undeformed beams along the normal direction (ND). The step sizes of 100 and 50 nm were used in the large and the small maps, respectively. Confidence index of the EBSD maps were greater than 0.1. Average Euler angles of both beams were $(1.4^\circ, 3.1^\circ$ and $8.0^\circ)$ in Bunge convention.

Table 1

Beam dimensions; t_{ext} , t_{int} , w , l , y , z are the thickness at the exterior and the interior surfaces, width, length, moment arm and the offset of the contact point from the center line of the beam, respectively.

	t_{ext} (μm)	t_{int} (μm)	w (μm)	l (μm)	y (μm)	z (μm)
Beam a	4.6 ± 0.1	5.7 ± 0.1	15.0 ± 0.4	18.4 ± 0.3	12.1 ± 0.1	1.5 ± 0.1
Beam b	4.5 ± 0.2	5.9 ± 0.1	15.0 ± 0.4	15.9 ± 0.3	5.2 ± 0.1	1.6 ± 0.1

Dimensions are measured using scanning electron microscope. Beams a and b refer to the beams with moment arms of 12.1 ± 0.1 and $5.2 \pm 0.1 \mu\text{m}$, respectively.

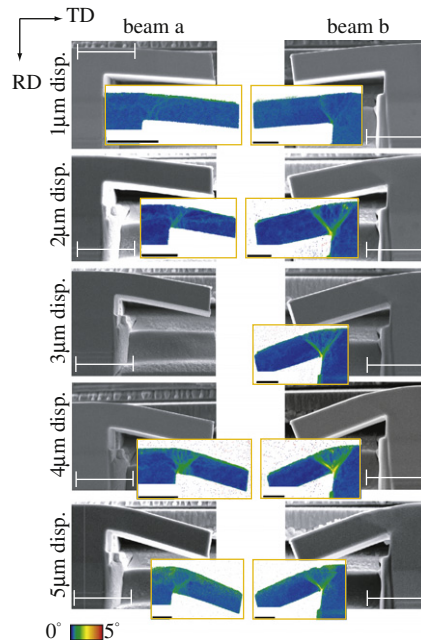


Fig. 3. SEM images and Kernel average misorientation (KAM) maps of beams a and b after deformation. Beams a and b refer to the beams with moment arms of 12.1 ± 0.1 and $5.2 \pm 0.1 \mu\text{m}$, respectively. The EBSD measurement of beam a after 3 μm displacement is not shown in this figure because of the significant amount of drift in that measurement. All the scale bars have 10 μm length. The confidence index is 0.1 for all the KAM maps.

2.2. Experimental results

Fig. 3 shows the SEM pictures of the beams after five steps of loading. The indentation of the beam surfaces are observed (maximum contact radius of the indent was 1.6 μm on beam b). However, the indentation signs allow repeatable positioning of the indenter before each loading step. Moreover, the indentation signs reveal sliding of the indenter tip over the beam surface as the beams rotate after 4 and 3 μm displacements of beams a and b, respectively. Furthermore, grid-like regular patterns on the top surface of the both beams are observed (SEM images in Fig. 4). The dislocations leaving the crystal during bending from the top surface of the beams produce the grid-like patterns since the patterns are not parallel to the FIB milling direction.

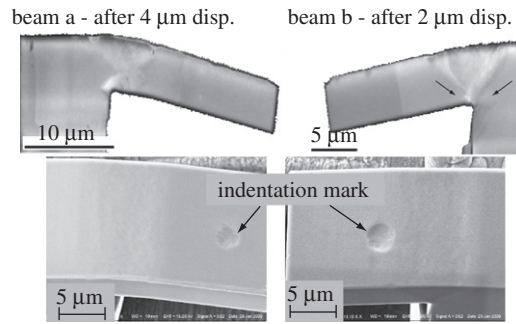


Fig. 4. EBSD image quality maps and SEM images at 70° tilt position of beams a and b at approximately the same magnitude of strain. Beams a and b refer to the beams with moment arms of 12.1 ± 0.1 and 5.2 ± 0.1 μm , respectively.

Table 2

Amount of the total displacement, total angular rotation of the beams (θ), vector components of the rotation axes along the rolling (RD), transverse (TD) and normal (ND) directions and flow stress σ at the end of loading are shown.

Beam	Tot. disp. (μm)	θ (deg)	RD comp.	TD comp.	ND comp.	σ (MPa)
Beam a	1	3.6 ± 0.2	0.03 ± 0.02	0.16 ± 0.02	0.98 ± 0.02	258
Beam a	2	6.1 ± 0.1	0.04 ± 0.05	0.18 ± 0.03	0.98 ± 0.01	251
Beam a	3	9.1 ± 0.1	0.05 ± 0.05	0.13 ± 0.02	0.98 ± 0.01	242
Beam a	4	13.5 ± 0.2	0.07 ± 0.01	0.11 ± 0.02	0.99 ± 0.01	229
Beam a	5	16.18 ± 0.2	0.05 ± 0.04	0.11 ± 0.01	0.99 ± 0.01	217
Beam b	1	6.9 ± 0.2	0.05 ± 0.05	0.12 ± 0.01	0.99 ± 0.01	261
Beam b	2	11.1 ± 0.2	0.02 ± 0.02	0.06 ± 0.04	1.00 ± 0.01	246
Beam b	3	16.4 ± 0.4	0.03 ± 0.01	0.08 ± 0.01	1.00 ± 0.01	209
Beam b	4	19.7 ± 0.1	0.05 ± 0.05	0.08 ± 0.08	1.00 ± 0.01	173
Beam b	5	20.8 ± 0.3	0.03 ± 0.01	0.09 ± 0.01	1.00 ± 0.01	–

Beams a and b refer to the beams with moment arms of 12.1 ± 0.1 and 5.2 ± 0.1 , respectively.

The kernel average misorientation (KAM) maps in Fig. 3 reveal the following important observations: (i) Misorientations in the beams are inhomogeneously distributed. (ii) Orientation changes occur nearly at the same locations after each displacement increment. (iii) Strong shear localizations can be noticed from the orientation changes along the slip plane traces. Local single slip (or coplanar double slip) is observed rather than an expected combined multiple slip for the cube orientation. (iv) Shear localizations initiate at the radius of the rounded inside corner and they progress through the thickness of the beams. (v) Shear localizations have a greater magnitude and a greater volume fraction in beam b with a shorter moment arm than in beam a. (vi) Misorientation axes between the points at undeformed regions inside the beams are calculated. The major components of the misorientation axes are along the normal direction (Table 2) hence, the other moments are negligibly small compared to the bending moment.

Fig. 4 shows the image quality maps at approximately the same magnitude of strains for both beams. The EBSD image quality maps may also be used as a qualitative indicator of strain (Wilkinson and Hirsch, 1997). However, the contrast and the brightness of image quality maps does not only depend on strain hence, maps provide only qualitative information about the strains. The distribution of strains in the image quality map of beam a resembles an ideal bending geometry more than beam b in which significant shear strains along the slip plane traces are observed. Further, a relatively weak bending strain distribution in beam b can also be noticed from careful inspection of the image quality maps (indicated with arrows in Fig. 4).

Figs. 5 and 6 show the force displacement and the bending stress vs. displacement curves. Bending stress is calculated using Eqs. (1) and (2) in which f , y , y_{corr} , R , θ , w and t refer to force, moment arm, geometrically corrected moment arm, radius of the indenter tool, measured angular rotation of the beams after each test (Table 2), width and thickness of the beams (Table 1), respectively. The factor 4 in Eq. (1) results in an average bending stress over the half of the thickness of the beam assuming an ideal bending stress distribution:

$$\sigma = \frac{4fy_{corr}}{wt^2} \quad (1)$$

$$y_{corr} = y - R \tan \theta \quad (2)$$

Force displacement curves reveal the following: (i) The stiffness of the beams remain the same until the displacements of 5 and 4 μm of beams a and b, respectively. Later, there is significant change in the elastic stiffness of beams a and b due to

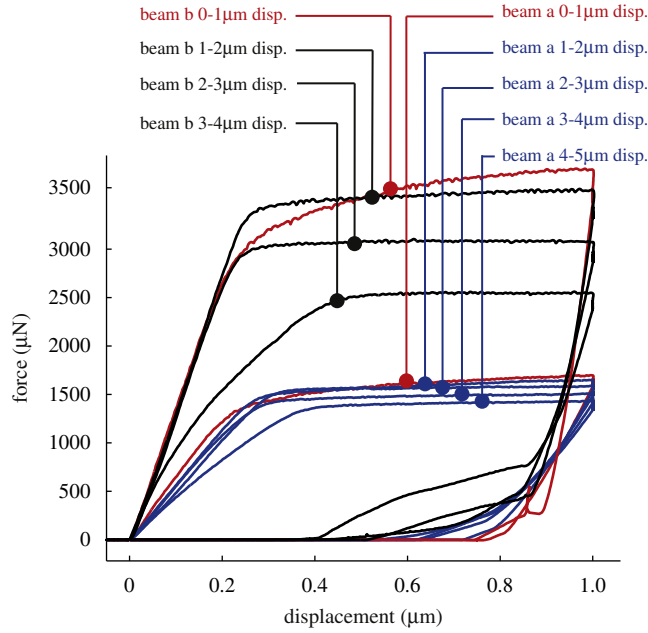


Fig. 5. Experimental indenter force vs. indenter displacement curves of beams a and b. Beams a and b refer to the beams with moment arms of 12.1 ± 0.1 and $5.2 \pm 0.1 \mu\text{m}$, respectively.

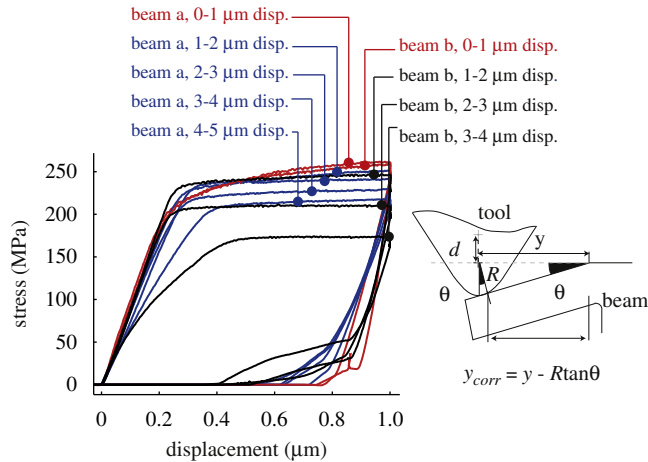


Fig. 6. Bending stress vs. displacement curves of the beams at certain displacement intervals. The small sketch at the top right corner illustrates the correction used for the moment arms. y , y_{corr} , R and θ refer to moment arm, geometrically corrected moment arm, radius of the indenter tip and total measured angular rotation of the beam (Table 2), respectively. Beams a and b refer to the beams with moment arms of 12.1 ± 0.1 and $5.2 \pm 0.1 \mu\text{m}$, respectively.

sliding of the indenter tip over the beam surface. (ii) The constant drifts in the forces between the end of loading and the beginning of reloading of the same beam are due to a repeatable decrease in the moment arm between each unloading and reloading cycle. (iii) The slopes of the first force displacement curves in the elastic-plastic regime (indicated in red color in Fig. 5) are greater than the following displacement increments. (iv) The drops/rises (small bumps) in the loading curves may be linked to the dislocations leaving the crystal since these force transients are not present in the linear elastic regime.

Average flow stresses (stresses at the end of loading) are 245 ± 13 and 239 ± 27 MPa for beams a and b, respectively, excluding the curves that have drastic changes in the elastic stiffness (between 4–5 and 3–4 μm displacement increments for beams a and b, respectively). The stresses at the end of loading are considered as the flow stress in this work. There is

nearly 19% maximum difference in the elastic stiffness of the remaining beams which is due to the change in the contact point after unloading and reloading.

3. Single crystal finite element model

The implicit finite element procedure seeks for the displacement field iteratively until the discretized principle of virtual work is satisfied weakly within a prescribed tolerance. Eq. (3) shows the virtual work principle applied to a body at the deformed reference that is discretized with a shape function, N_i . Internal stress, P_{ij} , is in equilibrium with body forces p_i on body Ω and surface tractions t_i over surface $d\Omega$:

$$\int_{\Omega} \nabla_x N_{ij}^T P_{ij} dV = \int_{d\Omega} N_i^T t_i dA + \int_{\Omega} N_i^T \rho p_i dV \quad (3)$$

Finite element software provides the deformation gradient at the material points after the displacement field iteration.

3.1. Deformation kinematics

The total deformation gradient¹ F_{ij} is decomposed multiplicatively into its elastic, F_{ij}^e , and plastic, F_{ij}^p , parts (Lee, 1969). The plastic part of the deformation gradient maps the undeformed vectors to an imaginary configuration referred as intermediate or relaxed configuration. Crystal orientation retains the same after plastic deformation that enforces isochoric (zero volume change) plastic deformation:

$$F_{ij} = F_{im}^e F_{mj}^p, \quad \det(F_{ij}^p) = 1 \quad (4)$$

The elastic part of the deformation accounts for the stretch, U_{ij} , and the rotation, Ω_{ij} , of the lattice:

$$F_{ij}^e = \Omega_{im} U_{mj} \quad (5)$$

The right elastic Cauchy tensor, C_{ij}^e , is given by

$$C_{ij}^e = F_{mi}^e F_{mj}^e \quad (6)$$

The plastic velocity gradient, \tilde{L}_{ij}^p , refers to the tensorial sum of the shear rates, γ^α , over the slip systems α in the intermediate configuration. The dyadic product of slip direction, \tilde{s}_i^α , and slip plane normal, \tilde{n}_j^α , is known as Schmid tensor, \tilde{S}_{ij}^α :

$$\tilde{L}_{ij}^p = \dot{F}^p_{im} F_{mj}^{p-1} \quad (7)$$

$$\tilde{L}_{ij}^p = \sum_{\alpha=1}^{12} \gamma^\alpha \tilde{s}_i^\alpha \tilde{n}_j^\alpha \quad (8)$$

$$\tilde{s}_i^\alpha \tilde{n}_j^\alpha = \tilde{S}_{ij}^\alpha \quad (9)$$

The work conjugate resolved shear stress, τ^α , to the slip rate, γ^α , is given by

$$\tau^\alpha = F_{mi}^e F_{mn}^e \tilde{P}_{nj} \tilde{S}_{ij}^\alpha \quad (10)$$

The 2nd Piola–Kirchhoff stress, \tilde{P}_{ij} , the driving stress for the dislocation slip in the crystal frame, results from elastic stretching of the crystal lattice. \tilde{P}_{ij} is estimated using the elasticity tensor, $\tilde{\zeta}_{ijkl}$, with the Green–Lagrange definition of strain for large deformations, \tilde{E}_{ij}^e , in

$$\tilde{P}_{ij} = \tilde{\zeta}_{ijkl} \tilde{E}_{kl}^e \quad (11)$$

$$\tilde{E}_{ij}^e = \frac{F_{mi}^e F_{mj}^e - \delta_{ij}}{2} \quad (12)$$

2nd Piola–Kirchhoff stress, \tilde{P}_{mn} , is pushed forward to the deformed reference to obtain the stress state at the deformed configuration, Cauchy stress, P_{ij} :

$$P_{ij} = F_{im}^e \tilde{P}_{mn} F_{jn}^e / \det(F_{ij}^e) \quad (13)$$

¹ Index notation is used throughout the text; rank of the tensors can be deduced from the indices. Summation is performed over the repeated indices; $a_i = B_{im} c_m = \sum_{m=1}^3 B_{im} c_m$. Kronecker delta is represented by the symbol δ_{ij} . Dyadic product is represented with $C_{ij} = a \otimes b = a_i b_j$.

Table 3
Slip systems in the undeformed crystal reference for fcc metals.

Slip planes, n_i^c	(111)			$(\bar{1}\bar{1}1)$			$(\bar{1}11)$			$(1\bar{1}1)$		
Slip directions, s_i^c	[01 $\bar{1}$]	$\bar{1}$ 01]	[1 $\bar{1}$ 0]	[0 $\bar{1}\bar{1}$]	[101]	$\bar{1}$ 10]	[01 $\bar{1}$]	[101]	$\bar{1}$ 10]	[0 $\bar{1}\bar{1}$]	$\bar{1}$ 01]	[110]

3.2. Constitutive laws

Elastic anisotropy for cubic materials is included using the three stiffness parameters, C_{11} , C_{12} , C_{44} , to construct elasticity tensor, ζ_{ijkl}^c , in the crystal frame:

$$\zeta_{ijkl}^c = C_{12}\delta_{ij}\delta_{kl} + C_{44}(\delta_{ik}\delta_{jl} + \delta_{il}\delta_{jk}) \quad (14)$$

$$+ (C_{11} - C_{12} - 2C_{44})\delta_{ir}\delta_{jr}\delta_{kr}\delta_{lr} \quad (15)$$

Table 3 shows 12 distinct slip systems for single phase fcc metal in the crystal frame.² The slip direction, $s_j^{c\alpha}$, slip plane normal, $n_i^{c\alpha}$, and the elasticity tensor, ζ_{ijkl}^c , are transformed from the crystal frame to the reference (and intermediate) configuration only once at the beginning of the calculations.

The shear rate on slip system α is calculated using a classical power law relation in which $\gamma_0^{\alpha}, m, \tau_c^{\alpha}$ and τ^{α} are referred as the reference shear rate, slip rate sensitivity parameter, slip resistance (may be referred as slip system hardness, critical resolved shear strength or threshold shear strength) and the resolved shear stress, respectively.

$$\dot{\gamma}^{\alpha} = \gamma_0^{\alpha} \left| \frac{\tau^{\alpha}}{\tau_c^{\alpha}} \right|^{1/m} \text{sign}(\tau^{\alpha}) \quad (16)$$

The hardening rate at the slip system α is linearly proportional to the absolute amount of the shear rate on any slip system, β . The hardening matrix, h_{β}^{α} , includes the latent hardening effect through the latent hardening matrix, $H^{\alpha\beta}$. Latent hardening refers to dislocation slip on slip system β causing hardening of slip system α . In Eq. (19), q is the latent hardening coefficient (Asaro and Rice, 1977) and A is a 3 by 3 matrix of ones (Kalidindi et al., 1992):

$$\dot{\tau}_c^{\alpha} = \sum_{\beta=1}^{12} h_{\beta}^{\alpha} |\dot{\gamma}^{\beta}| \quad (17)$$

$$h_{\beta}^{\alpha} = H^{\alpha\beta} h^{\beta} \quad (18)$$

$$H^{\alpha\beta} = \begin{pmatrix} A & qA & qA & qA \\ qA & A & qA & qA \\ qA & qA & A & qA \\ qA & qA & qA & A \end{pmatrix} \quad (19)$$

The single slip hardening rate is estimated using three different slip hardening parameters; h_0 , a and τ_c^{sat} , that refer to the reference hardening rate, the hardening exponent and the saturation value for the slip resistance:

$$h^{\beta} = h_0 \left(1 - \frac{\tau_c^{\beta}}{\tau_c^{sat}} \right)^a \quad (20)$$

The two level implicit integration method to solve the above constitutive equations, developed by Maniatty et al. (1992), is revisited in the Appendix part. The method is implemented in Hypela2, a material user subroutine of MSC-Marc finite element software. The material tangent is calculated by the perturbation method as proposed by Kalidindi et al. (1992).

Table 4 shows the values of the numerical parameters used in the simulations from Kalidindi et al. (1992) and elastic constants from Reid (1973). Bulk single crystal properties in Table 4 are frequently used in literature for well annealed copper.

3.3. Effects of beam geometry and friction

The effect of the taper along beam width, the radius of the rounded inside corner and the friction coefficient on the force displacement behavior of beam a are investigated with eight (2^3) parameter combinations using a two level factorial analysis (DeVor et al., 2007). The relative effects of taper, friction and radius on the force displacement response are estimated using the area under the force displacement curves as the output parameter. The values of radius, friction coefficient and the taper angle used in the simulations are shown in Table 5. A dry friction coefficient of 0.4 that is greater than the common friction coefficient for metal to diamond contact (0.15) and a slip resistance of 16 MPa are used.

² $s_j^{c\alpha}$ and $n_i^{c\alpha}$: the superscript c indicate the crystal frame, α represents the slip system and subscript j refer to the j th component of vector.

Table 4

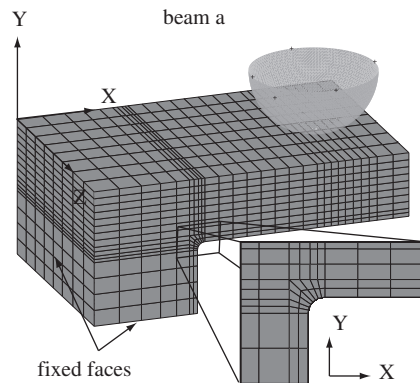
Numerical parameters that are used in the simulations.

$\dot{\gamma}_0$ (1/s)	m	τ_c^0 (MPa)	C_{11} (MPa)	C_{12} (MPa)	C_{44} (MPa)	h_0 (MPa)	τ_c^{sat} (MPa)	a	q
0.001	0.012	16/44	168 400	121 400	75 400	180	148	2.25	1.4

Two different slip resistances were used in Section 3.4.

Table 5The values for taper along the beam width, friction coefficient between the tool and the sample surface and radius of the rounded inside corner used in the 2^3 factorial analysis are shown.

Beam	Id	Radius (μm)	Fric. coeff.	Taper (deg)	$f.d$ ($\mu\text{N } \mu\text{m}$)	$\bar{f.d}$
Beam a	p1	0	0	0	49 684	0.56
Beam a	p2	0.6	0	0	89 681	0.99
Beam a	p3	0	0.4	0	49 684	0.55
Beam a	p4	0.6	0.4	0	89 681	0.99
Beam a	p5	0	0	2	74 369	0.83
Beam a	p6	0.6	0	2	89 808	1.00
Beam a	p7	0	0.4	2	74 369	0.83
Beam a	p8	0.6	0.4	2	89 809	1.00

Standard order of variables is used in the analysis DeVor et al. (2007). The area of the resulting force displacement curves and the normalized magnitudes are indicated with $f.d$ and $\bar{f.d}$, respectively.**Fig. 7.** The mesh used for beam a with solid brick type of elements and boundary conditions.

The normalized magnitudes of main effects (DeVor et al., 2007) for the radius of the rounded inside corner, the friction coefficient and the taper angle are 0.15, 0.00 and 0.07, respectively. The friction between the indenter and the beam surface has negligible influence on the force displacement curves. The radius has 45% greater effect on the force displacement curves than the taper. In addition, interaction (DeVor et al., 2007) exists only between the parameters; radius of the rounded inside corner and the taper angle. Therefore, the effect of taper on the force displacement curve strongly depends on the magnitude of the radius.

3.4. Simulation results

The actual dimensions of beams and the moment arms (Table 1) are used in the simulations. The models for beam a and beam b consist of 2528 and 2208 eight node solid brick elements, respectively. The mesh and the boundary conditions for beam a are shown in Fig. 7. Euler angles before loading (271.4° , 3.1° , 98°) and (88.6° , 3.1° , 262°) for beam a and beam b, respectively. The coordinate frames (X,Y,Z) of the finite element models of beams a and b are different than that of the EBSD maps (RD, TD, ND), Fig. 2 hence, crystal orientations of the beams are transformed to their corresponding finite element references. The indenter is modeled as a rigid sphere with $5 \mu\text{m}$ radius. The friction and the taper are ignored in the beam models.

Fig. 8 shows the force displacement curves during the first displacement increments. The simulated elastic stiffness of the beams are approximately 20% greater than the experimentally measured ones. That difference is not due to the angular misalignment of the indenter axis from ideal (which is not considered in the model) since, 20% change in the elastic

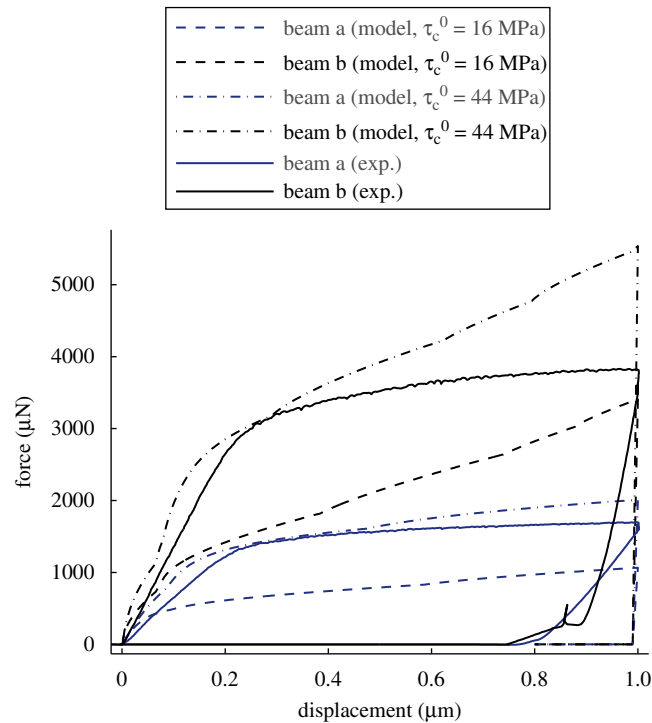


Fig. 8. The experimentally obtained and simulated (for initial slip resistances, τ_c^0 , of 16 and 44 MPa) indenter force vs. indenter displacement curves of beams a and b. Beams a and b refer to the beams with moment arms of 12.1 ± 0.1 and 5.2 ± 0.1 μm , respectively.

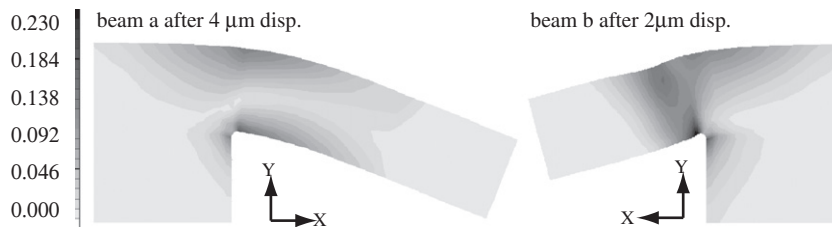


Fig. 9. Simulated Von Mises equivalent total strains on the side of the beams a and b after test 4 and test 2, respectively. The simulated strain distributions provide comparison to the EBSD image quality maps shown in Fig. 4. Beams a and b refer to the beams with moment arms of 12.1 ± 0.1 and 5.2 ± 0.1 μm , respectively.

stiffness corresponds to an unreasonable amount of (36.8°) angular misalignment. The top surfaces of the beams have a curved shape due to the fish-eye geometry of FIB over long milling distances (manufacturing artifact). Therefore, the use of the average of external and internal thicknesses (as indicated in Fig. 1) in the model causes overestimation of the thickness and results in a stiffer than actual model. However, any artificial scaling to correct that difference is avoided.

The experimental magnitude of force at the onset of plasticity is approximately 100–120% greater than the simulated forces for a slip resistance of 16 MPa. The difference in the flow strength may be related with the initial microstructure (i.e. initial dislocation density). For reliable comparison of simulated and experimental force displacement curves, simulations were repeated for 44 MPa slip resistance since a greater slip system hardness would lead to a more saturated hardening response.

The simulated slopes of force displacement curves in the plastic flow regime (not exactly equal but proportional to the strain hardening rates) are approximately 1.6 and 3.3 times higher than the experimentally measured values, respectively, for beams a and b. The simulations overestimate the hardening inside the beams.

Simulations show that beam b undergoes greater strain hardening than beam a. The additional shearing of beam b due to short moment arm causes greater number of active slip systems in beam b compared to beam a. This leads to greater interactions between the slip systems hence, the greater strain hardening of beam b.

Fig. 9 shows the equivalent strain distributions on the side surface of the beams. Both the moment arm and the radius of the rounded inside corner effect the resulting strain distributions as in the experiments, Fig. 4. In addition, the deformed region underneath the indenter interferes with the bent region in beam b.

4. Discussion

Plane strain bending is accomplished for the dimensions of the cube oriented cantilever beams. Regular dislocation patterns that are observed along the width of the beams (Fig. 4) indicate the presence of plane strain inside the beams. Indentation of the top surface of the beams is observed for the selected beam dimensions. The maximum contact radius of the indent ($\approx 1.6 \mu\text{m}$ on beam b) corresponds to a plastically deformed volume of nearly $8.3 \mu\text{m}^3$ and the corresponding bent volume is approximately $191 \mu\text{m}^3$ ($\approx wt^2/2$, from Fig. 4). The maximum plastically deformed region underneath the indent constitutes approximately 4.3% of the bent volume. Therefore, the effect of indentation on the force displacement is expected to be very low and reliable mechanical strength can be measured by cantilever beam bending tests.

Bending is achieved by shearing along the slip directions. The shear stress is the driving force for the dislocation glide and it is maximum at 45° plane with respect to the horizontal axis (TD in Fig. 3). Therefore, slip systems nearest to that plane are the primary slip systems, Fig. 3.

Shear localizations along the maximum shear stress direction occur as a combined effect of the moment arm and the radius of the rounded inside corner. Shearing along slip plane traces through the thickness of the beams (as observed from the misorientation maps) is only possible with the aid of the radius of the rounded inside corner acting as a stress raiser. Moreover, misorientation maps revealed greater fraction of shear localizations for beam b which has a shorter moment arm. Therefore, the radius of the rounded inside corner and the moment arm significantly influence the distribution of misorientations (Fig. 3) and strains (Fig. 4). In addition, the repulsive forces between the moving dislocations and the attractive forces from the surfaces (image dislocations) on the mobile dislocations are believed to enhance the formation of shear localizations.

Cube orientation is stable during microscale bending in contrast to macroscopic tests (Raabe et al., 2004). Orientation changes occur nearly at the same locations after each displacement increment (Fig. 3) hence, same nucleation sites for the generation of dislocations are expected.

The symmetric nature of cube orientation allows in-plane bending with negligible amount of twist. The twist components of the misorientation axis are negligible compared to bending (Table 2). Imperfections regarding the experiments (i.e. tool alignment) leads to slight twisting of the beams. However, for cube orientation provides sufficient number of active slip systems to compensate the changes in the external boundary constraints and internal local differences in the slip resistance.

The change in the moment arm, as an external boundary constraint, causes a 2.7% and 6.7% drops in the measured flow stresses in between displacement intervals of beams a and b, respectively. The constant drops might be linked with a repeatable change in the contact point which shows the strong effect of the moment arm on the measured forces.

Average flow stresses (245 ± 13 and 239 ± 27 MPa, respectively, for beams a and b) are significantly higher than the tensile test results of cube oriented copper (less than 50 MPa at 5% elongation from Takeuchi, 1975). The measured flow stresses are within the range of the literature findings for copper cantilever beams (for $5 \mu\text{m}$ thickness from Motz et al., 2005: 260–281 MPa, and for $4.23 \mu\text{m}$ thickness from Demir et al., 2010: 180–200 MPa). The disagreement between the measured flow stresses and the literature results may be related to the difference in the sample geometry (i.e. magnitude of radius) and/or the initial crystal orientation.

The first stress displacement curves of both beams have greater slopes in the elastic–plastic regime compared to the latter curves, Fig. 6. This may be due to the indentation of the surface during first tests. At later displacement increments, the deformed region underneath the indent gets enough hard and the contact radius of the indents do not change until the sliding of the indenter tip.

The crystal plasticity model captures the essential features of microscale bending. The simulated, (Fig. 9), and measured, (Fig. 4), strain distributions are in qualitative agreement.

The simulated force displacement match well the experiments when the initial slip resistance of 44 MPa is used. This is greater than the slip resistance of well annealed copper (16 MPa) which may be linked with the initial microstructure. Strain gradients are not measured before bending (Fig. 2) hence, the initial increase in the flow strength might not be associated with the strain gradients. Moreover, force displacement curves are linear in the elastic regime which indicates no early transition to plastic flow. Therefore, the initial strengthening may not be associated with the geometrically necessary dislocations that may possibly stem from early plasticity.

The magnitudes of the slopes of the force displacement curves in the plastic flow regime (will be referred as hardening rates) in the experiments are significantly lower compared to the simulated slopes. In the simulations common bulk single crystal material properties are used and the hardening contribution of the strain gradients is not incorporated to the model. However, the simulated slope of the force displacement curves are 1.6 and 3.3 times greater, respectively, for beams a and b, compared to the experiments. This suggests negligible amount of experimentally measured strain gradient hardening for single crystal beams with $5 \mu\text{m}$ thickness. These results contradict with the literature findings (Stolken and Evans, 1998; Motz et al., 2005) since, strain gradient hardening is expected for beams with $5 \mu\text{m}$ thickness. Lattice rotations are confined to a smaller region in cantilever beam bending than in a uniform bending situation. Moreover, greater strain gradients exist in the shear localizations than in a bent lattice. Although a greater strain gradient hardening is expected in cantilever beam bending compared to uniform bending, the experimentally measured hardening rates are lower than the simulated bulk material behavior. Therefore, strain hardening is believed to be controlled by the statistical dislocation reactions in the microscale beams instead of the strain gradients.

The dislocations leaving the crystal (strain softening) may cause softening of the beams. The size of the beams are even smaller than the substructure sizes that are observed in bulk crystal copper after straining (i.e. dislocation cells have approximately 10 μm size Kocks and Mecking, 2003). The surfaces in such small dimensions may alter hardening behavior in comparison to bulk material behavior. Active slip systems are always inclined with respect to the horizontal (beam axis) since the primary slip systems are the ones that are closest to the maximum shear stress direction. Therefore, dislocations during microscale bending may leave the crystal before they get stored that might cause the lower strain hardening compared to bulk hardening behavior of single crystals. This effect is believed to have a minor role on the hardening behavior of the beams since the beams are already bent which gives rise to a demand for the geometrically necessary dislocations.

5. Conclusions

Bending can be used as a reliable testing method to find the mechanical strength of materials at micrometer scale. Several important findings are outlined as follows:

- Bending without twist can be achieved for cube oriented microcantilever beams.
- Bending takes the form of localized shearing as the moment arm gets shorter. The moment arm must be greater than two times the size of the thickness to obtain a pure bending state.
- Local stress concentrations, in particular the radius of the rounded inside corner, may alter bending to localized shearing. The deviation from bending increases as the moment arm gets smaller.
- Indentation signs may be used to set or determine the moment arm with a negligible influence on the mechanics of wide beams.
- Simulations revealed the negligible influence of the friction between the indenter and the beam surface on the simulated force displacement curves. In addition, the thickness variation along the width of the beams has 45% less effect than the radius of the rounded inside corner.
- Slip resistance of 44 MPa rather than 16 MPa is estimated for single crystal copper by the simulations. The difference is linked with the initial microstructure of the beams.
- The finite element model using conventional crystal plasticity with bulk single crystal properties, resulted in greater strain hardening in the simulations than the experiments. The simulations validate the importance of statistical hardening mechanisms in comparison to the strain gradient based hardening.
- The experimentally observed low strain hardening behavior compared to the simulated bulk material response may also be partly related to the leaving of dislocations through the surfaces of the beams (annihilation/strain softening).

Appendix A. Crystal plasticity solution method

Given: F_{ij} , F_{ijt} , F_{ijt}^p , τ_{ct}^α .

Find: F_{ij}^p , τ_c^α .

Following Maniatty et al. (1992), F_{ij}^p and τ_c^α are determined using a two-level implicit iterative procedure. At the inner level of iterations, the solution for F_{ij}^p is sought by Newton Raphson method for a fixed value of slip resistance, τ_c^α . Once, the correct value of F_{ij}^p is determined, kinematically coupled quantities can be calculated: e.g. F_{ij}^e , E_{ij} , \dot{P}_{ij} , τ^α , $\dot{\gamma}^\alpha$ and \tilde{L}_{ij}^p using the Eqs. (4), (12), (11), (10), (16) and (8), respectively. The outer level of iterations is to find the correct value for τ_c^α .

\tilde{L}_{ij}^p can also be estimated by Euler backward difference approximation from the differential equation in Eq. (7).

$$F_{ijt}^p = F_{ij}^p - F_{ij}^p \Delta t \quad (21)$$

$$F_{imt}^p F_{mj}^{p-1} = \delta_{ij} - F_{in}^p F_{nj}^{p-1} \Delta t \quad (22)$$

$$= \delta_{ij} - \tilde{L}_{ij}^p \Delta t$$

$$\tilde{L}_{ij}^p = \frac{\delta_{ij} - F_{imt}^p F_{mj}^{p-1}}{\Delta t} \quad (23)$$

In Eq. (21) F_{ijt}^p belongs to the previous time increment³ and Δt is the corresponding time step between the deformation increments. The residual, ψ_{ij} , is calculated from the difference between the Euler backward difference approximation, Eq. (23) and the \tilde{L}_{ij}^p that is estimated from the constitutive relations, Eq. (8). The penalty term with the penalty factor λ_p in Eq. (24) enforces zero volume change during plastic deformation. The magnitude of the penalty

³ The variables that belong to the previous time step are indicated with the subscript 't' and the remaining variables without any indicator belong to the current time step ($t + \Delta t$) for simplicity.

factor, λ_p , is 1000.

$$\psi_{ij} = \underbrace{\sum_{\alpha=1}^{12} \gamma^{\alpha} \tilde{s}_i^{\alpha} \tilde{n}_j^{\alpha}}_{\psi_{ij}^1} - \underbrace{\frac{\delta_{ij} - F_{im}^p F_{mj}^{p-1}}{\Delta t}}_{\psi_{ij}^2} + \underbrace{\lambda_p [\det(F_{ij}^p) - 1]}_{\psi_{ij}^3} \delta_{ij} \quad (24)$$

At the inner level of iterations, the correct value of ${}^k F_{ij}^p$ is calculated using Newton–Raphson (NR) iterative scheme. In Eqs. (25), (26) and (28) the superscripts k and $k + 1$ indicate the estimates at the end of the k and $k + 1$ inner level iterations Eq. (25). The increment in the plastic deformation gradient, ${}^k \Delta F_{ij}^p$, is obtained, Eq. (27) considering only the first term in Taylor expansion of the residual around ${}^k F_{ij}^p$ and setting ${}^{k+1} \psi_{ij}$ to zero as Eq. (26).

$${}^{k+1} \psi_{ij} = {}^k \psi_{ij} + \frac{d[{}^k \psi_{ij}]}{d[{}^k F_{mn}^p]} {}^k \Delta F_{mn}^p \quad (25)$$

$${}^{k+1} \psi_{ij} = 0 \quad (26)$$

$${}^k \Delta F_{ij}^p = -J_{ijmn}^{-1} {}^k \psi_{mn}, \quad J_{ijmn} = \frac{d[{}^k \psi_{ij}]}{d[{}^k F_{mn}^p]} \quad (27)$$

$${}^{k+1} F_{ij}^p = {}^k F_{ij}^p + {}^k \Delta F_{ij}^p \quad (28)$$

The differential of the residual, ψ_{ij} , with respect to F_{kl}^p refers to the Jacobian, J_{ijkl} , the tangent used in the NR scheme. A fully plastic initial guess is used to start iterations, Eq. (29):

$${}^0 F_{ij}^p = F_{im}^{-1} F_{mj} \quad (29)$$

$\frac{d[\psi_{ij}^1]}{d[F_{kl}^p]}$ in Eq. (24) is calculated in order to estimate the Jacobian. Therefore, $\frac{d[\gamma^{\alpha}]}{d[\tau^{\alpha}]}$ is estimated from Eq. (16), as in Eq. (31).

$$\frac{d[\psi_{ij}^1]}{d[F_{kl}^p]} = \frac{d[\gamma^{\alpha}]}{d[\tau^{\alpha}]} \frac{d[\tau^{\alpha}]}{d[F_{kl}^p]} \tilde{s}_{ij}^{\alpha} \quad (30)$$

$$\frac{d[\gamma^{\alpha}]}{d[\tau^{\alpha}]} = \frac{\gamma_0}{\tau_0^{\alpha} m} \left| \frac{\tau^{\alpha}}{\tau_0^{\alpha}} \right|^{1/m-1} \quad (31)$$

In addition, the derivative of the resolved shear stress with respect to F_{ij}^p , $\frac{d[\tau^{\alpha}]}{d[F_{kl}^p]}$ has to be calculated. Hence, τ^{α} in Eq. (32) is expressed in terms of F_{ij}^p using Eq. (10) together with the Eqs. (6), (11) and (12)

$$\tau^{\alpha} = F_{mi}^{p-1} C_{mn} F_{np}^{p-1} \tilde{\zeta}_{pjru} \tilde{E}_{ru}^e \tilde{s}_{ij}^{\alpha} \quad (32)$$

$$\tilde{E}_{ru}^e = \frac{F_{sr}^{p-1} C_{st} F_{tu}^{p-1} - \delta_{ru}}{2} \quad (33)$$

The partial derivative of the resolved shear stress in Eq. (32) with respect to F_{ij}^p becomes⁴

$$\frac{d[\tau^{\alpha}]}{d[F_{kl}^p]} \tilde{s}_{ij}^{\alpha} = \frac{1}{2} \left\{ \left(\frac{d[F_{mi}^{p-1}]}{d[F_{kl}^p]} C_{mn} F_{np}^{p-1} + F_{mi}^{p-1} C_{mn} \frac{d[F_{np}^{p-1}]}{d[F_{kl}^p]} \right) \tilde{\zeta}_{pjru} (C_{ru}^e - \delta_{ru}) \tilde{s}_{ij}^{\alpha} + C_{ip}^e \tilde{\zeta}_{pjru} \left(\frac{d[F_{sr}^{p-1}]}{d[F_{kl}^p]} C_{st} F_{tu}^{p-1} + F_{sr}^{p-1} C_{st} \frac{d[F_{tu}^{p-1}]}{d[F_{kl}^p]} \right) \tilde{s}_{ij}^{\alpha} \right\} \quad (34)$$

$$\frac{d[\tau^{\alpha}]}{d[F_{kl}^p]} \tilde{s}_{ij}^{\alpha} = \frac{1}{2} \left\{ (-F_{ml}^{p-1} C_{kp}^e + C_{mk}^e F_{pl}^{p-1}) \tilde{\zeta}_{pnrs} (C_{rs}^e - \delta_{rs}) + C_{mp}^e \tilde{\zeta}_{pnrs} (F_{rl}^{p-1} C_{ks}^e + C_{rk}^e F_{sl}^{p-1}) \right\} \tilde{s}_{mn}^{\alpha} \tilde{s}_{ij}^{\alpha} \quad (35)$$

Jacobian, J_{ijkl} , for the NR scheme⁵ is calculated using Eq. (38).

$$\frac{d[\psi_{ij}^2]}{d[F_{kl}^p]} = -F_{im}^p F_{mk}^{p-1} F_{ij}^{p-1} / \Delta t \quad (36)$$

$$\frac{d[\psi_{ij}^3]}{d[F_{kl}^p]} = \delta_{ij} \lambda_p \det(F_{ij}^p) F_{kl}^{p-T} \quad (37)$$

$$J_{ijkl} = \frac{d[\psi_{ij}^1]}{d[F_{kl}^p]} + \frac{d[\psi_{ij}^2]}{d[F_{kl}^p]} + \frac{d[\psi_{ij}^3]}{d[F_{kl}^p]} \quad (38)$$

⁴ $F_{im} F_{mj}^{-1} = \delta_{ij}$ and $dF_{im} F_{mj}^{-1} + F_{im} dF_{mj}^{-1} = 0$, hence $dF_{ij}^{-1} = -F_{im}^{-1} dF_{mn} F_{nj}^{-1}$.

⁵ The derivative of the determinant is the adjugate matrix $\frac{d(\det(F_{ij}))}{d[F_{kl}]} = \det(F_{ij}) F_{kl}^{-T}$.

The inner loop converges when ${}^k F_{kl}^p$ gives a solution which has a L^2 -norm of the residual, $\|\psi_{ij}\|$, is lower than the tolerance. Next in the outer loop, the increment of the slip resistance is estimated using the converged values of the shear rates according to Eq. (17). In Eqs. (39) and (40) the superscripts r and $r+1$ indicate the estimates for the slip resistance at the end of r and $r+1$ outer level iterations. The outer level iteration continues until the relative change in the slip resistance (${}^r \tau_c^\alpha \Delta t / {}^r \tau_c^\alpha$) becomes less than the prescribed tolerance. 10^{-6} is used as the relative tolerance value for both the inner and the outer loops. The slip resistance at the previous time step, ${}^0 \tau_c^\alpha$, is used to start the iterations, Eq. (40).

$${}^{r+1} \tau_c^\alpha = {}^r \tau_c^\alpha + {}^r \dot{\tau}_c^\alpha \Delta t \quad (39)$$

$${}^0 \tau_c^\alpha = \tau_{ct}^\alpha \quad (40)$$

The numerical algorithm used is as follows:

1. Calculate the initial guess, ${}^0 F_{ij}^p$, using Eq. (29).
2. Calculate F_{ij}^e , E_{ij} , \tilde{P}_{ij} , τ^α and γ^α by Eqs. (4), (12), (11), (10) and (16), respectively.
3. Compute residual, ${}^k \psi_{ij}$, from Eq. (24) and its norm $\|{}^k \psi_{ij}\|$.
 - (i) if $\|{}^k \psi_{ij}\| < \text{tolerance}$: converged (go to step 6).
 - (ii) elseif $k \neq 1$ and $\|{}^k \psi_{ij}\| > \text{tolerance}$ and $\|{}^k \psi_{ij}\| > \|{}^{k-1} \psi_{ij}\|$: scale back ${}^k F_{ij}^p$ using the scaling factor ζ . A magnitude of 0.75 for ζ is used in the simulations.

$${}^k F_{ij}^p = \zeta^{k-1} F_{ij}^p + (1-\zeta) {}^k F_{ij}^p \quad (41)$$
 - (iii) else start/continue iterations using the Jacobian in Eq. (27), (go back to step 2).
4. Calculate ${}^{k+1} F_{ij}^p$, using Eq. (28).
5. Go back to step 2 (inner loop).
6. Update slip resistivity, ${}^{r+1} \tau_c^\alpha$ with Eq. (39).
7. Go back to step 2 (outer loop).
8. Calculate and store the output variables: misorientations, sum of shear rates, etc.

References

- Asaro, R.J., Rice, J.R., 1977. Strain localization in ductile single-crystals. *Journal of the Mechanics and Physics of Solids* 25 (5), 309–338.
- Ashby, M.F., 1970. Deformation of plastically non-Homogeneous materials. *Philosophical Magazine* 21 (170), 399.
- DeVor, R.E., Chang, T.-h., Sutherland, J.W., 2007. *Statistical Quality Design and Control: Contemporary Concepts and Methods*. Pearson, Prentice Hall, Upper Saddle River, NJ.
- Demir, E., Raabe, D., Roters, F., 2010. The mechanical size effect as a mean-field breakdown phenomenon: example of microscale single crystal beam bending. *Acta Materialia* 58 (5), 1876–1886.
- Fleck, N.A., Muller, G.M., Ashby, M.F., Hutchinson, J.W., 1994. Strain gradient plasticity—theory and experiment. *Acta Metallurgica Et Materialia* 42 (2), 475–487.
- Gong, J.C., Wilkinson, A.J., 2009. Anisotropy in the plastic flow properties of single-crystal alpha titanium determined from micro-cantilever beams. *Acta Materialia* 57 (19), 5693–5705.
- Greer, J.R., Oliver, W.C., Nix, W.D., 2005. Size dependence of mechanical properties of gold at the micron scale in the absence of strain gradients. *Acta Materialia* 53 (6), 1821–1830.
- Kalidindi, S.R., Bronkhorst, C.A., Anand, L., 1992. Crystallographic texture evolution in bulk deformation processing of fcc metals. *Journal of the Mechanics and Physics of Solids* 40 (3), 537–569.
- Kiener, D., Motz, C., Rester, M., Jenko, M., Dehm, G., 2007. FIB damage of Cu and possible consequences for miniaturized mechanical tests. *Materials Science and Engineering A—Structural Materials Properties Microstructure and Processing* 459 (1–2), 262–272.
- Kocks, U.F., Mecking, H., 2003. Physics and phenomenology of strain hardening: the FCC case. *Progress in Materials Science* 48 (3), 171–273.
- Lee, E.H., 1969. Elastic–plastic deformation at finite strains. *Transactions of the ASME. Series E, Journal of Applied Mechanics* 36 (1), 1–6.
- Maniatty, A.M., Dawson, P.R., Lee, Y.S., 1992. A time integration algorithm for elastoviscoplastic cubic-crystals applied to modeling polycrystalline deformation. *International Journal for Numerical Methods in Engineering* 35 (8), 1565–1588.
- Motz, C., Schoberl, T., Pippan, R., 2005. Mechanical properties of micro-sized copper bending beams machined by the focused ion beam technique. *Acta Materialia* 53 (15), 4269–4279.
- Nix, W.D., Gao, H.J., 1998. Indentation size effects in crystalline materials: a law for strain gradient plasticity. *Journal of the Mechanics and Physics of Solids* 46 (3), 411–425.
- Nix, W.D., Greer, J.R., Feng, G., Lilleodden, E.T., 2007. Deformation at the nanometer and micrometer length scales: effects of strain gradients and dislocation starvation. *Thin Solid Films* 515 (6), 3152–3157.
- Nye, J.F., 1953. Some geometrical relations in dislocated crystals. *Acta Metallurgica* 1, 153–162.
- Raabe, D., Zhao, Z., Roters, F., 2004. Study on the orientational stability of cube-oriented FCC crystals under plane strain by use of a texture component crystal plasticity finite element method. *Scripta Materialia* 50 (7), 1085–1090.
- Reid, C.N., 1973. *Deformation Geometry for Materials Scientists*. Pergamon Press, Oxford, New York.
- Shade, P.A., Wheeler, R., Choi, Y.S., Uchic, M.D., Dimiduk, D.M., Fraser, H.L., 2009. A combined experimental and simulation study to examine lateral constraint effects on microcompression of single-slip oriented single crystals. *Acta Materialia* 57 (15), 4580–4587.
- Shi, Z.F., Huang, B., Tan, H., Huang, Y., Zhang, T.Y., Wu, P.D., Hwang, K.C., Gao, H., 2008. Determination of the microscale stress–strain curve and strain gradient effect from the micro-bend of ultra-thin beams. *International Journal of Plasticity* 24 (9), 1606–1624.
- Stolken, J.S., Evans, A.G., 1998. A microbend test method for measuring the plasticity length scale. *Acta Materialia* 46 (14), 5109–5115.

- Takeuchi, T., 1975. Work-hardening of copper single-crystals with multiple glide orientations. *Transactions of the Japan Institute of Metals* 16 (10), 629–640.
- Uchic, M.D., Dimiduk, D.M., Wheeler, R., Shade, P.A., Fraser, H.L., 2006. Application of micro-sample testing to study fundamental aspects of plastic flow. *Scripta Materialia* 54 (5), 759–764.
- Volkert, C.A., Lilleodden, E.T., 2006. Size effects in the deformation of sub-micron Au columns. *Philosophical Magazine* 86 (33–35), 5567–5579.
- Wang, H., Hwang, K.C., Huang, Y., Wu, P.D., Liu, B., Ravichandran, G., Han, C.S., Gao, H., 2007. A conventional theory of strain gradient crystal plasticity based on the Taylor dislocation model. *International Journal of Plasticity* 23 (9), 1540–1554.
- Wilkinson, A.J., Hirsch, P.B., 1997. Electron diffraction based techniques in scanning electron microscopy of bulk materials. *Micron* 28 (4), 279–308.